

High-wavenumber steady solutions of two-dimensional Rayleigh–Bénard convection between stress-free boundaries

Alexander Takla¹ and Baole Wen^{2, a)}¹*Department of Physics and Department of Mathematics, University of Michigan, Ann Arbor, MI 48109, USA*²*Department of Mathematics, New York Institute of Technology, Old Westbury, NY 11568, USA; Department of Mathematics, University of Michigan, Ann Arbor, MI 48109, USA*

(Dated: 13 December 2022)

Recent investigations show that steady solutions share many features with the turbulent Rayleigh–Bénard convection (RBC) and form the state space skeleton of the turbulent dynamics. Previous computations of steady roll solutions in two-dimensional (2D) RBC between no-slip boundaries reveal that for fixed Rayleigh number Ra and Prandtl number Pr , the heat-flux-maximizing solution is always in the high-wavenumber regime. In this study, we explore the high-wavenumber steady convection roll solutions that bifurcate supercritically from the motionless conductive state for 2D RBC between stress-free boundaries. Our new computations confirm the existence of a local heat-flux-maximizing solution in the high-wavenumber regime. To elucidate the asymptotic properties of this solution, we perform computations over eight orders of magnitude in the Rayleigh number, $10^8 \leq Ra \leq 10^{16.5}$, and two orders of magnitude in the Prandtl number, $10^{-1} \leq Pr \leq 10^{3/2}$. The numerical results indicate that as $Ra \rightarrow \infty$, the local heat-flux-maximizing aspect ratio $\Gamma_{loc}^* \simeq Ra^{-1/4}$, the Nusselt number $Nu(\Gamma_{loc}^*) \simeq Ra^{0.29}$, and the Reynolds number $Re(\Gamma_{loc}^*) \simeq Pr^{-1} Ra^{2/5}$, with all prefactors depending on Pr . Moreover, the interior flow of the local Nu -maximizing solution can be well described by an analytical heat-exchanger solution, and the connection to the high-wavenumber asymptotic solution given by Blennerhassett & Bassom (IMA J. Appl. Math., vol. 52, 1994, 51–77) is discussed. With a fixed aspect ratio $0.06 \leq \Gamma \leq \pi/5$ at $Pr = 1$, however, our computations show that as Ra increases, the steady rolls converge to the semi-analytical asymptotic solutions constructed by Chini & Cox (Phys. Fluids, vol. 21, 2009, 083603), with scalings $Nu \sim Ra^{1/3}$ and $Re \sim Pr^{-1} Ra^{2/3}$. Finally, a phase diagram is delineated to gain a panorama of steady solutions in the high-Rayleigh-number-wavenumber plane.

I. INTRODUCTION

Buoyancy-driven convection—flows resulting from density variations in the presence of gravity—is a key environmental and technological process with broad applications in engineering heat transport^{1,2}, weather and climate science^{3–5}, ocean dynamics⁶, and stellar physics^{7–10}. Rayleigh–Bénard convection, the buoyancy-driven flow in a fluid layer heated from below and cooled from above, has been investigated extensively since the 1910s¹¹, in large part because it is recognized as the simplest scenario to study such phenomena. As the imposed temperature gradient increases, Rayleigh–Bénard convection exhibits rich nonlinear dynamics and thereby provides an ideal physical and mathematical setting for studying instabilities, bifurcations, pattern formation, and turbulence^{7,8,12}.

Rayleigh–Bénard convection undergoes a sequence of bifurcations as the Rayleigh number Ra , the normalized temperature drop across the layer, is increased. In a sufficiently wide, two-dimensional (2D) horizontal fluid layer uniformly heated from below and cooled from above, convection rolls set in via a stationary bifurcation of the conduction state at a critical Rayleigh number depending on the boundary conditions^{11,13}. As Rayleigh number increases in a certain range above the critical value, the steady rolls strengthen but remain stable. Then, periodic and quasiperiodic flows, and zonal flows; finally, convection becomes turbulent at the large Rayleigh numbers^{14–17}.

Recently, steady convective flows have become the subject of intense scrutiny since certain steady states capture aspects of turbulent convection^{18–27}. Although steady coherent states are not typically caught in large- Ra experiments or simulations as they are dynamically unstable, they and their unstable manifolds are part of the global attractor for the infinite-dimensional dynamical system. As has also been observed for unstable coherent states in shear flows^{28–34}, turbulent trajectories spend the majority of their lifetimes in the neighborhoods of these equilibrium solutions and other types of exact coherent states like time-periodic solutions and thereby inherit some quantitative features²³. Moreover, recent study on a truncated model of Rayleigh–Bénard convection suggests steady states may maximize the heat transport enhancement factor, i.e. the Nusselt number Nu , among all stable or unstable flows³⁵. Indeed, all the known investigations of steady solutions in Rayleigh–Bénard convection and its variations reveal that certain steady convective states transport heat more efficiently than turbulence at comparable parameters^{22,24,25,27}. It is still an open question whether steady solutions can saturate the upper bounds on heat transport derived from variational analysis^{36–39} or at least achieve the same scaling with the bounds.

In this manuscript, we study high-wavenumber steady roll solutions bifurcating supercritically from the conductive state for 2D Rayleigh–Bénard convection between stress-free boundaries. Previous investigations in low- and moderate-wavenumber regimes indicate that as $Ra \rightarrow \infty$, steady roll solutions for each aspect ratio Γ show a clear asymptotic scaling $Nu \sim Ra^{1/3}$ uniformly in Prandtl number Pr , with a Γ -

^{a)} Author to whom correspondence should be addressed: bwen@nyit.edu

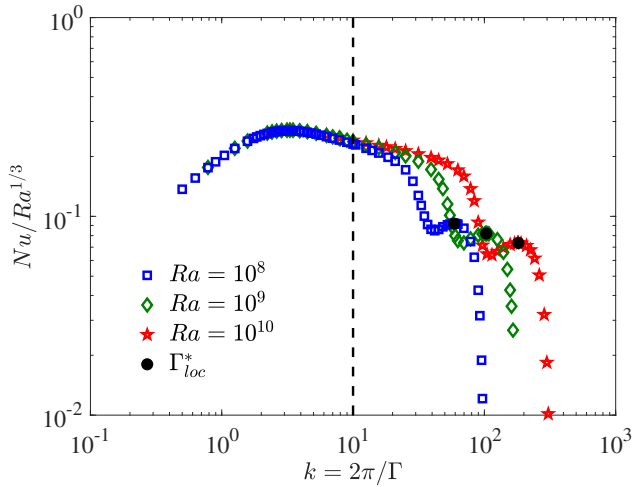


FIG. 1. Compensated plot of Nu vs wavenumber $k = 2\pi/\Gamma$ for steady convection rolls with $Pr = 1$ between stress-free boundaries. Low- and moderate-wavenumber solutions, points left of the dashed line ($k \leq 10$), are from Wen et al.²². Highlighted points are Γ_{loc}^* that locally maximizes $Nu(\Gamma)$ for fixed Ra and Pr , similar to the no-slip case²⁵.

dependent prefactor; and at each Ra and Pr , the aspect ratio of rolls maximizing Nu approaches $\Gamma \approx 1.9$ ^{22,40}. However, recent computations of steady rolls with no-slip boundary conditions exhibit significant differences from the stress-free case^{18,19,25}. For fixed $\Gamma = 2$ at $Pr = 1$, the no-slip steady rolls display the scaling $Nu \sim Ra^{1/4}$ as $Ra \rightarrow \infty$, while for fixed Ra and $Pr = 1$, the dependence $Nu(\Gamma)$ has multiple local maxima in the high-wavenumber regime with the Nu -maximizing aspect ratio $\Gamma^* \sim Ra^{-0.20}$ approaching zero rather than a constant and $Nu(\Gamma^*) \sim Ra^{1/3}$ as $Ra \rightarrow \infty$ ²⁵. Hence, it is natural to wonder whether there exist local maxima of $Nu(\Gamma)$ in the high-wavenumber regime for stress-free steady rolls; if so, whether these solutions can achieve a higher asymptotic scaling than $1/3$.

Our new computations of high-wavenumber steady roll solutions in figure 1 reveal that for fixed Ra and Pr , there does exist a local maximum for $Nu(\Gamma)$ in 2D Rayleigh–Bénard convection between stress-free boundaries. Therefore, in this investigation we will explore the asymptotic flow structure and heat transport of this local Nu -maximizing solution. Moreover, a systematic study on the steady roll solutions at $10 \leq k \leq k_c$, where $k_c \sim Ra^{1/4}$ is the wavenumber of the narrowest marginally stable mode from the linear stability analysis of the conduction solution, will be performed to gain a panorama of steady solutions in the Ra - k plane. Inspired by our numerical results, we propose an analytical solution to model the interior flows of the high-wavenumber steady rolls. Its connections to the asymptotic solutions given by Blennerhassett & Bassom⁴¹ for high-wavenumber Rayleigh–Bénard convection and by Chini & Cox⁴⁰ for strongly nonlinear Rayleigh–Bénard convection will be discussed. A phase diagram of steady solutions in high- Ra - k plane will be delineated.

The rest of this paper is organized as follows. In the next section, we formulate the standard mathematical model of

Rayleigh–Bénard convection and outline the numerical methods to solve the steady-version equations. The numerical results will be described and analyzed in section III and our conclusions will be given in section IV.

II. PROBLEM FORMATION AND COMPUTATIONAL METHODOLOGY

Consider a 2D fluid layer in a domain $(x, z) \in [0, \Gamma] \times [0, 1]$ that is heated from below at $z = 0$ and cooled from above at $z = 1$. Following Rayleigh¹¹, we model the thermal convection using the Boussinesq equation

$$(\partial_t \mathbf{u} + \mathbf{u} \cdot \nabla \mathbf{u}) = -\nabla p + (Pr/Ra)^{1/2} \nabla^2 \mathbf{u} + T \hat{\mathbf{z}}, \quad (1a)$$

$$\nabla \cdot \mathbf{u} = 0, \quad (1b)$$

$$\partial_t T + \mathbf{u} \cdot \nabla T = (PrRa)^{-1/2} \nabla^2 T, \quad (1c)$$

where $\mathbf{u} = u\hat{\mathbf{x}} + w\hat{\mathbf{z}}$ is the velocity field, p is the pressure, and T is the temperature. Here the system has been non-dimensionalized using the layer thickness h , the temperature drop Δ from the lower wall to the upper one, the free-fall velocity $U_f = \sqrt{g\alpha h\Delta}$ where g is the gravitational acceleration and α is the thermal expansion coefficient, and the free-fall time h/U_f . The relevant three dimensionless parameters governing (1) are the aspect ratio Γ , the Prandtl number $Pr = \nu/\kappa$, i.e. the ratio of the kinematic viscosity ν to the thermal diffusivity κ , and the Rayleigh number $Ra = g\alpha h^3 \Delta / (\kappa\nu)$, i.e. the normalized temperature drop across the layer.

At the top and bottom boundaries, the temperature field satisfies isothermal boundary conditions, and the velocity field satisfies no-penetration and stress-free boundary conditions:

$$T|_{z=0} = 1, \quad T|_{z=1} = 0, \quad w|_{z=0,1} = 0, \quad \text{and} \quad \partial_z u|_{z=0,1} = 0. \quad (2)$$

All variables are Γ periodic in x . In such a domain, the conduction state becomes linearly unstable at a critical Rayleigh number $Ra_c = 27\pi^4/4$, at which a roll pair with the critical horizontal period $\Gamma_c = 2\sqrt{2}$ bifurcates supercritically¹¹. In the limit $Ra \rightarrow \infty$, the horizontal period of the narrowest marginally stable roll pair decreases as $2\pi Ra^{-1/4}$, while for finite Pr the horizontal period of the fastest-growing linearly unstable mode decreases as $O(Ra^{-1/8})$.

Two primary quantities of interest in Rayleigh–Bénard convection are the heat transport enhancement factor, i.e. the Nusselt number $Nu = 1 + (PrRa)^{1/2} \langle wT \rangle$, and the bulk Reynolds number based on root-mean-squared velocity, which in dimensionless terms is $Re = (Ra/Pr)^{1/2} \langle |\mathbf{u}|^2 \rangle^{1/2}$.

Following the previous work^{21,22,25}, we compute the steady ($\partial_t = 0$) solutions of (1) using a vorticity–stream function formulation,

$$\partial_z \psi \partial_x \omega - \partial_x \psi \partial_z \omega = (Pr/Ra)^{1/2} \nabla^2 \omega + \partial_x \theta, \quad (3a)$$

$$\nabla^2 \psi = -\omega, \quad (3b)$$

$$\partial_z \psi \partial_x \theta - \partial_x \psi \partial_z \theta = -\partial_x \psi + (PrRa)^{-1/2} \nabla^2 \theta, \quad (3c)$$

where the stream function ψ is defined by $\mathbf{u} = \partial_z \psi \hat{\mathbf{x}} - \partial_x \psi \hat{\mathbf{z}}$, the (negative) scalar vorticity is $\omega = \partial_x w - \partial_z u = -\nabla^2 \psi$, and

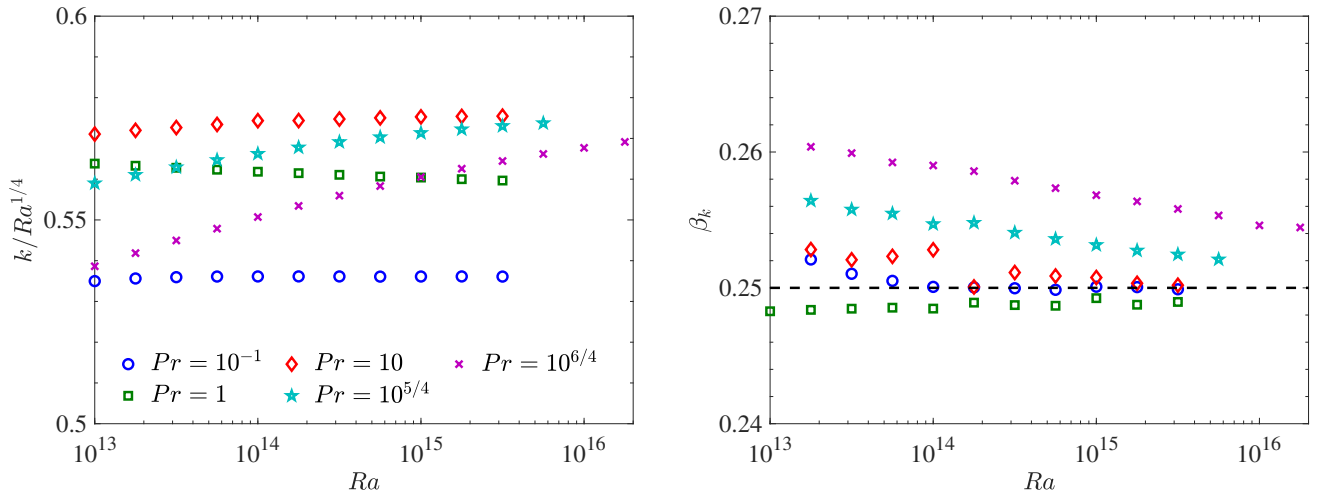


FIG. 2. Left: Compensated plot of the fundamental horizontal wavenumber $k = 2\pi/\Gamma$ vs Ra for the aspect ratio Γ_{loc}^* that maximizes $Nu(\Gamma)$ locally over a variety of Pr . As $Ra \rightarrow \infty$, $k_{loc}^* = 2\pi/\Gamma_{loc}^* \simeq c_k(Pr)Ra^{1/4}$ and convergence occurs more slowly at larger Pr . Right: Finite-difference approximations of the local scaling exponent $\beta_k = d(\log k_{loc}^*)/d(\log Ra)$.

θ is the deviation of the temperature field from the conduction state, i.e. $\theta = T - (1 - z)$. From the fixed-temperature and stress-free conditions (2), θ , ψ , and ω satisfy Γ -periodic boundary conditions in x and homogeneous Dirichlet boundary conditions at $z = 0, 1$. In this investigation, (3) is solved numerically using a Newton–GMRES (generalized minimal residual) iterative scheme developed by Wen et al.²². The spatial discretization is achieved using a Fourier series in x and a Chebyshev collocation method in z ^{42,43}. We refer to the reference²² for more details of the numerical methods.

III. RESULTS

We first compute the local Nu -maximizing solutions over eight orders of magnitude in the Rayleigh number, $10^8 \leq Ra \leq 10^{16.5}$, and two orders of magnitude in the Prandtl number, $10^{-1} \leq Pr \leq 10^{3/2}$. Computations are performed for fixed (Ra, Pr) at high wavenumbers to precisely find Γ_{loc}^* that locally maximizes $Nu(\Gamma)$ (cf. figure 1). For $Pr < 10^{-1}$, our computations indicate the local Nu -maximizing solution does not exist. Moreover, we also compute the steady roll solutions with fixed aspect ratios $\Gamma = 0.06, 0.08, 0.1, 0.2, 0.4, 0.5$, and $\pi/5$ by increasing Ra to reach the asymptotic transport regime, compensating the previous work²² which focuses on $\Gamma \geq \pi/5$.

A. Local Nu -maximizing solutions

Figure 2 shows the Ra - and Pr -dependences of the wavenumber $k_{loc}^* = 2\pi/\Gamma_{loc}^*$ for local Nu -maximizing solutions. As in the no-slip case with Prandtl number unity²⁵, $k_{loc}^* \simeq c_k(Pr)Ra^{1/4}$ with $c_k \approx 0.55$ for $10^{-1} \leq Pr \leq 10^{3/2}$ in the case of stress-free velocity conditions. This suggests that Γ_{loc}^* follows the same $Ra^{-1/4}$ scaling as the narrowest

marginally stable mode and at fixed Ra , the Prandtl number Pr has a weakly impact on the magnitude of Γ_{loc}^* .

Figure 3 displays the structure of the local Nu -maximizing solutions at $Ra = 10^{15}$ for $Pr = 0.1, 1$, and 10 . In the interior (far away from the top and bottom boundaries), the steady convection rolls at $\Gamma = \Gamma_{loc}^*$ exhibit a similar flow structure for different Pr : the fluctuations of the temperature field T , the stream function field ψ , and the vorticity field ω are dominated by the first harmonic, and ψ and ω are nearly z -independent (figure 4). It should be noted that similar flow features are also observed at high-wavenumber steady solutions in porous medium Rayleigh–Bénard convection^{20,44}. This type of steady interior flow could be well approximated using the following analytical heat-exchanger solution:

$$T = -A\sqrt{\frac{Pr}{Ra}}k^3 \cos kx + \frac{1}{2} \left(\frac{k^4}{Ra} + 1 \right) - \frac{k^4}{Ra}z, \quad (4a)$$

$$\psi = A \sin kx, \quad (4b)$$

$$\omega = Ak^2 \sin kx, \quad (4c)$$

where the coefficient A is constant. In this solution, the horizontal diffusion between neighboring up- and downwelling plumes balances the vertical advection of a background linear temperature gradient. Moreover, it can be shown that (4) satisfies the governing equations (3) exactly except the top and bottom boundary conditions. By comparing the horizontal-mean temperature \bar{T} , the steady roll numerical solution agrees closely with the analytical heat-exchanger solution in the interior at $\Gamma = \Gamma_{loc}^*$ and $Pr = 1$ (figure 4). Actually, our computations reveal that the convection rolls always exhibit the heat-exchanger flow structure in the interior for $k_h < k < k_c = Ra^{1/4}$, where k_h is to be determined.

Between the boundary layer and the bulk there exists a recirculation zone in each convection roll with $\Gamma = \Gamma_{loc}^*$ (figure 3). As Pr increases, the recirculation zone moves toward the walls and the area gets smaller. Moreover, our numer-

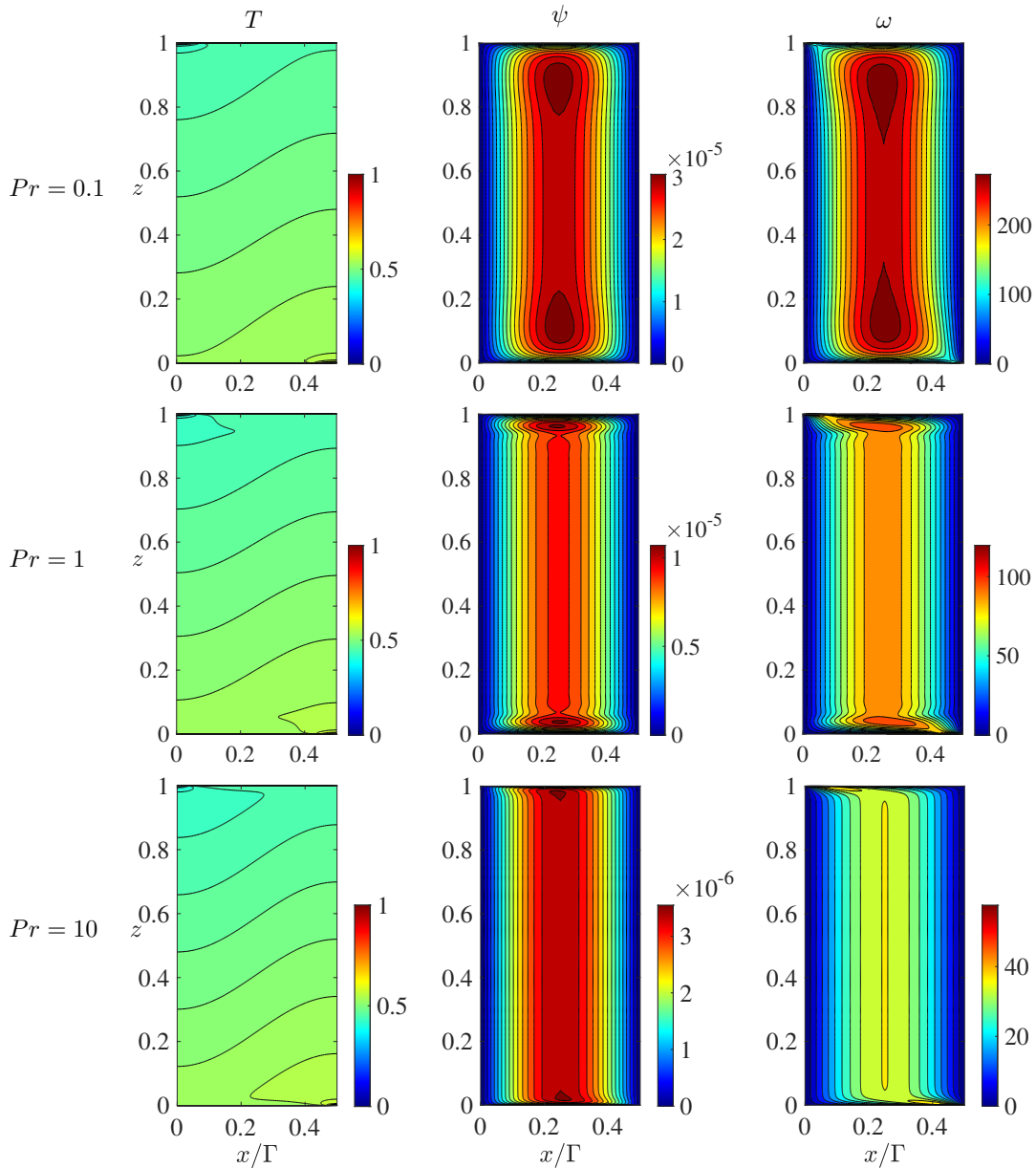


FIG. 3. Contours of (from left to right) T , ψ , and ω for solutions at $Ra = 10^{15}$ with (from top to bottom) $\Gamma = \Gamma_{loc}^* = 0.0020841$, 0.0019938 , and 0.0019422 and $Pr = 0.1$, 1 , and 10 . Only the convection roll with counterclockwise circulation is plotted due to the reflection symmetry about $x = \Gamma/2$. The extremum ψ values (in free-fall scale), which occur at the center of the recirculation near the top and bottom boundaries, are 3.17×10^{-5} , 1.08×10^{-5} , and 3.59×10^{-6} , respectively, for $Pr = 0.1$, 1 , and 10 ; while in thermal diffusion scale they become 3.17×10^2 , 3.42×10^2 , and 3.59×10^2 , respectively. For increasing Pr , the area of the recirculation gets smaller.

ical results also indicate that for local Nu -maximizing solutions with fixed Pr , the boundary layer in the temperature field scales approximately as $Ra^{-0.29}$, and a thicker boundary layer in both the stream function and vorticity fields scales approximately as $Ra^{-0.1}$ (figure 5). Interestingly, after appropriate rescaling the horizontal-mean temperature profiles collapse near the bottom boundary (figure 5), while the horizontal-mean stream function and vorticity profiles over a single convection roll collapse near the bottom boundary and in the interior, as shown in figure 5 and suggested by equations (4b)

and (4c).

It is worth noting that the local Nu -maximizing solutions reported here exhibit very similar flow features with the wall-to-wall optimal flow under fixed-entrophy-budget scenario^{45,46}, i.e. the steady incompressible flow with a given amount of entrophy budget maximizing the heat transport between isothermal walls. For instance, for fixed-entrophy problem in wall-to-wall optimal transport the interior flow is dominated by a single Fourier mode and a recirculation zone emerges between the boundary layers and the bulk at large Péclet number.

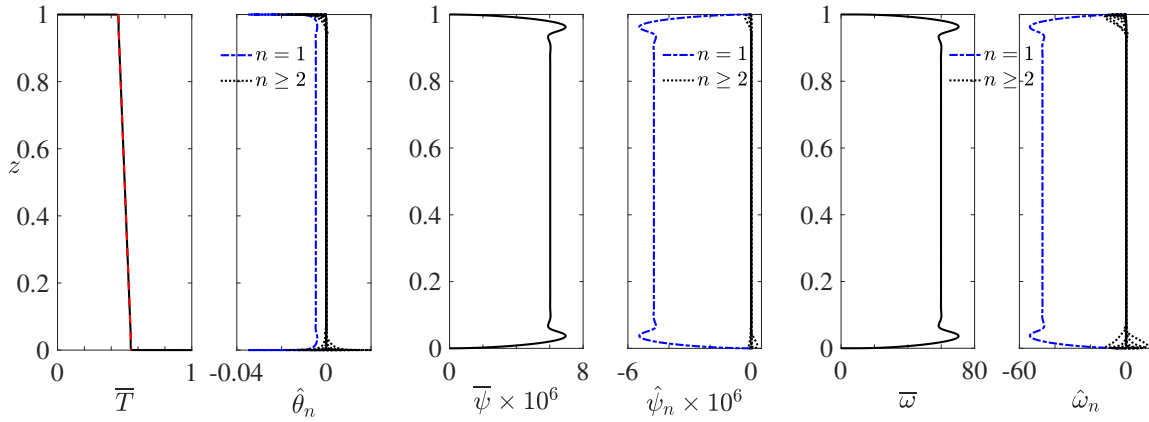


FIG. 4. The z -dependent Fourier components of the solution at $Ra = 10^{15}$ and $Pr = 1$ with $\Gamma = \Gamma_{loc}^* = 0.0019938$. The horizontal-mean components \bar{T} , $\bar{\psi}$, and $\bar{\omega}$ are from a single convection roll with counterclockwise circulation. The horizontal-mean temperature in the interior agrees closely with the analytical heat-exchanger solution (4) (red dashed line). The interior flow of the local Nu -maximizing solutions at $Pr = 0.1$ and 10 exhibits similar spectra structures as in the case of $Pr = 1$.

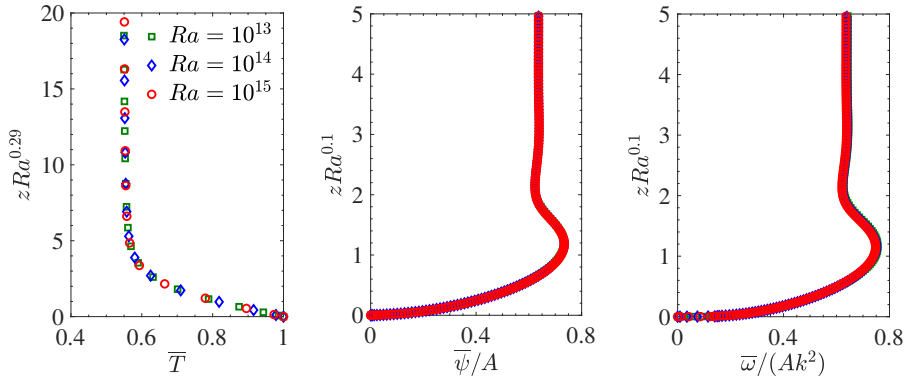


FIG. 5. Scaled mean profiles near the lower boundary for solutions at $Pr = 1$ with $\Gamma = \Gamma_{loc}^*$. For $Ra = 10^{13}$, 10^{14} , and 10^{15} , $\Gamma = \Gamma_{loc}^* = 0.0062667$, 0.0035365 , and 0.0019938 , respectively. The horizontal-mean profiles are from a single convection roll with counterclockwise circulation. Near the boundary, the mean profiles of the local Nu -maximizing solutions at $Pr = 0.1$ and 10 exhibits the same scaling characteristics as in the case of $Pr = 1$.

Intriguingly, the Nu -maximized aspect ratio for optimal wall-to-wall transport with fixed entrophy scales as $Ra^{-0.254645}$, close to $\Gamma_{loc}^* \simeq Ra^{-0.25}$ presented here. Nevertheless, for wall-to-wall optimal transport the steady incompressible flow is not required to satisfy the momentum equation (1a), while the steady rolls computed here exactly satisfy the full Boussinesq equations (1).

Figure 6 shows the dependence of Nu on Ra for local Nu -maximizing solutions over a variety of Pr . Consistent with the left panel of figure 5 and as in the no-slip case with $Pr = 1$, Nu scales approximately as $c_n(Pr)Ra^{0.29}$. Although Γ_{loc}^* is weakly affected by the Prandtl number, the prefactor c_n (computed based on the highest- Ra data) increases approximately from 0.166 at $Pr = 0.1$ to 0.402 at $Pr = 10^{3/2}$ as a results of the decreasing size of flow recirculation near the boundary (figure 3). Figure 7 depicts the dependence of Re on Ra for local Nu -maximizing solutions. As in the no-slip case with $Pr = 1$, Re scales roughly as $c_r(Pr)Ra^{2/5}$ with c_r (computed based on the highest- Ra data) increasing approximately from

0.636 at $Pr = 0.1$ to 0.922 at $Pr = 10^{3/2}$. Moreover, our data also indicate that convergence of Nu and Re to their asymptotic scalings occurs more slowly when Pr is larger.

B. Connection to Blennerhassett–Bassom solution in diffusion scale

As mentioned in the introduction section, Blennerhassett & Bassom⁴¹ performed an asymptotic analysis to explore the nonlinear high-wavenumber Rayleigh–Bénard convection in a 2D domain. As the scales of diffusion time (h^2/κ) and velocity (κ/h) were utilized by Blennerhassett & Bassom⁴¹, in this subsection we compare their solution with our heat-exchanger solution (4) in the same scales for consistency.

Established on expanding the Rayleigh number as

$$Ra = k^4 + R_1 k^3 + \dots, \quad \text{as } k \rightarrow \infty, \quad (5)$$

the asymptotic analysis by Blennerhassett & Bassom⁴¹ gives

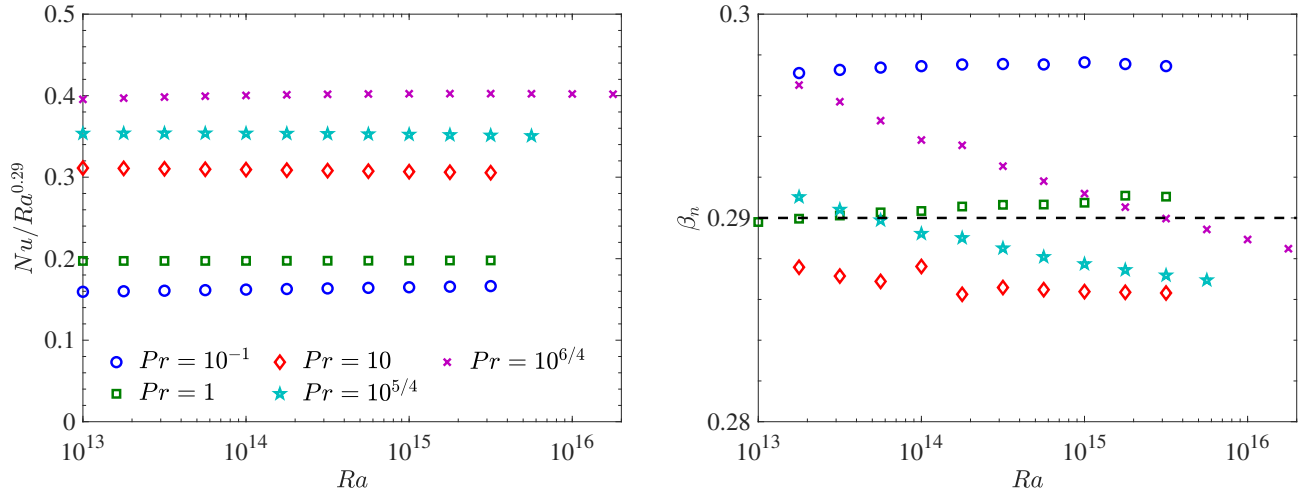


FIG. 6. Left: Compensated plot of Nu vs Ra at $\Gamma = \Gamma_{loc}^*$ over a variety of Pr . As $Ra \rightarrow \infty$, $Nu_{loc}^* \simeq c_n(Pr)Ra^{0.29}$ and convergence occurs more slowly at larger Pr . Right: Finite-difference approximations of the local scaling exponent $\beta_n = d(\log Nu_{loc}^*)/d(\log Ra)$.

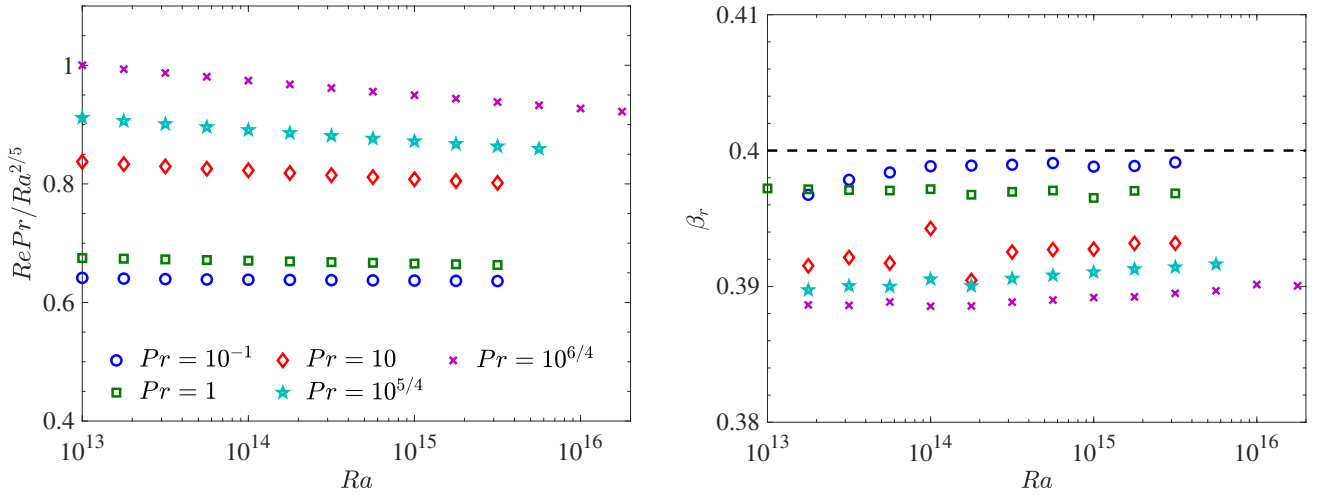


FIG. 7. Left: Compensated plot of Re vs Ra at $\Gamma = \Gamma_{loc}^*$ over a variety of Pr . As $Ra \rightarrow \infty$, the Péclet number $RePr \simeq c_r(Pr)Ra^{2/5}$ at $\Gamma = \Gamma_{loc}^*$ and convergence occurs more slowly at larger Pr . Right: Finite-difference approximations of the local scaling exponent $\beta_r = d(\log Re)/d(\log Ra)$.

the following expansions for the temperature and velocity fields in the core:

$$T = 1 - z + k^{-1}\bar{\theta}_1 + k^{-1}[\theta_{10}(z) + k^{-1}\theta_{11}(z) + \dots] \cos kx + k^{-3}\theta_{20}(z) \cos 2kx + \dots, \quad (6a)$$

$$u = [u_{10}(z) + k^{-1}u_{11}(z) + \dots] \sin kx + k^{-2}u_{20}(z) \sin 2kx + \dots, \quad (6b)$$

$$w = k[w_{10}(z) + k^{-1}w_{11}(z) + \dots] \cos kx + k^{-1}w_{20}(z) \cos 2kx + \dots. \quad (6c)$$

Substituting the known values of $\bar{\theta}_1 = R_1(z - 1/2)$, $\theta_{10} = 2\gamma$, $u_{10} = 0$, and $w_{10} = 2\gamma$ from Blennerhassett & Bassom⁴¹ and keeping only the leading order terms in k as $k \rightarrow \infty$, we obtain the following approximation for the temperature, stream

function, and vorticity in terms of diffusion velocity scale

$$T = 1 - z + k^{-1}R_1\left(z - \frac{1}{2}\right) + 2\gamma k^{-1} \cos kx, \quad (7a)$$

$$\psi = -2\gamma \sin kx, \quad (7b)$$

$$\omega = -2\gamma k^2 \sin kx. \quad (7c)$$

We rewrite the heat-exchanger solution (4) in diffusion velocity scale and substitute the expansion of Ra in (5),

$$T = 1 - z + k^{-1}R_1\left(z - \frac{1}{2}\right) \left(\frac{k}{k + R_1}\right) - A \sqrt{\frac{Pr}{k^4 + R_1 k^3}} k^3 \cos kx, \quad (8a)$$

$$\psi = A \sqrt{Pr(k^4 + R_1 k^3)} \sin kx, \quad (8b)$$

$$\omega = A \sqrt{Pr(k^4 + R_1 k^3)} k^2 \sin kx. \quad (8c)$$

As long as (i) $R_1 \sim O(1)$ so that $k/(k+R_1) \sim 1$ as $k \rightarrow \infty$ and (ii) $\gamma = -A\sqrt{Pr}k^2/2$, the heat exchanger solution (8) reduces to the Blennerhassett–Bassom solution (7). Actually, the leading order of the expansion (5), i.e. $Ra \sim k^4$, implies the Rayleigh number is expanded around the marginally stable mode $k_c \sim Ra^{1/4}$. Given the interior flow exhibits the heat-exchanger solution structure at high wavenumbers, the Blennerhassett–Bassom solution is accurate only for a small region below the neutral stability mode $k_c \sim Ra^{1/4}$.

C. Fixed- Γ solutions

At fixed aspect ratios independent of the size, our computations indicate that the steady convection rolls converge to the Chini–Cox solution eventually as $Ra \rightarrow \infty$. Since the Chini–Cox solution is Pr -independent in the leading order^{22,40}, in this subsection only the variations of convection roll solutions at $Pr = 1$ are discussed.

As shown in figure 8, for fixed $\Gamma = 0.06$ the convection rolls emerge at the critical Rayleigh number $Ra_c = k^4 = (2\pi/\Gamma)^4 \approx 1.2 \times 10^8$ due to a stationary bifurcation from the conduction state, and the interior exhibits the heat-exchanger flow structure in a certain region of $Ra > Ra_c$. At $Ra = 10^9$, $\Gamma = 0.06 \approx \Gamma_{loc}^* = 0.0608854$, so the convection roll still displays the typical flow features of the local Nu -maximizing solutions discussed in section III A. Namely, the interior flow is nearly z -independent and governed by a single Fourier mode, suggesting the horizontal diffusion between neighboring plumes balances the vertical advection of a background linear temperature gradient, and there exists a recirculation zone between the boundary layer and the bulk.

For increasing Ra , however, the interior flow becomes more inviscid and the convection roll solution transitions to the Chini–Cox solution gradually. As shown in figures 8 and 9, the temperature and vorticity fields become more homogenized in the core at higher Ra , i.e. $T \sim 1/2$ and $\sqrt{RaPr}\omega \sim \sqrt{C_n(k)}Ra^{2/3}$ with the coefficient C_n defined in the next paragraph. The diffusion is negligible unless within the thermal and vorticity layers on all four edges of a single convection roll. As confirmed in figure 10, the thicknesses of these layers, i.e. δ_z^T (thermal layer near the bottom), δ_x^T (thermal layer near the left edge), δ_z^ω (vorticity layer near the bottom), and δ_x^ω (vorticity layer near the left edge), all scale as $Ra^{-1/3}$. Unlike the temperature and vorticity fields, the rescaled stream function $\sqrt{RaPr}\psi/Ra^{2/3}$ at leading order in Ra is a relatively smooth function over the entire domain (figures 8 and 9) and becomes nearly invariant after sufficiently large Ra . We note that the recirculation zone disappears in the Chini–Cox flow, so the transport efficiency may be enhanced compared with the local Nu -maximizing solutions.

Figure 11 shows the dependence of Nu on Ra for steady convection rolls with fixed aspect ratios at $Pr = 1$. As Nu is compensated by $Ra^{1/3}$, the horizontal slope corresponds to the classical $1/3$ scaling, while the upward/downward slope corresponds to scaling exponents higher/lower than $1/3$. Consistent with the left panel of figure 10 and as also predicted by the asymptotic analysis of Chini & Cox⁴⁰, Nu scales as

$C_n(k)Ra^{1/3}$ with a decreasing prefactor C_n as k increases in the high-wavenumber regime. For $\Gamma = 0.06$, the compensated Nusselt number $Nu/Ra^{1/3}$ undergoes a non-monotonic variation with Ra , e.g. it reaches a local maximum slightly before $Ra = 10^9$, where $\Gamma = 0.06 \approx \Gamma_{loc}^* = 0.0608854$ with an approximate scaling exponent 0.29, and reduces to a local minimum around $Ra = 10^{10}$ due to the change of the flow pattern (figure 8). After $Ra \approx 10^{10}$, the local scaling exponent has a sharp rise and becomes higher again than $1/3$, but this upward trend does not mean that the convection starts to transition to the ‘ultimate’ $1/2$ scaling which claims that the heat transport becomes independent of the thermal diffusivity and kinematic viscosity of the working fluid as $Ra \rightarrow \infty$ ⁴⁷. In fact, for 2D Rayleigh–Bénard convection with stress-free boundary conditions it has been proved mathematically by Whitehead & Doering³⁹ that $Nu \leq Ra^{5/12}$ for all flow solutions whether steady, unsteady, turbulent, etc. Finally, as shown in figure 11, Nusselt number of the steady rolls with fixed aspect ratios converges to the classical $1/3$ scaling and the prefactor $C_n(k)$ of our computations agrees quantitatively with the asymptotic prediction by Chini & Cox⁴⁰.

Figure 12 shows the dependence of Re on Ra for steady convection rolls over $10 \leq k \leq 100\pi/3$ at $Pr = 1$. As predicted by the asymptotic analysis of Chini & Cox^{22,40}, Re scales as $C_r(k)Pr^{-1}Ra^{2/3}$ with a decreasing prefactor C_r as k increases in the high-wavenumber regime. Moreover, it is clear from figures 11 and 12 that the convergence of $Nu/Ra^{1/3}$ and $RePr/Ra^{2/3}$ is slower at higher k (smaller Γ) and Re reaches its asymptotic scaling sooner than Nu does, which are consistent with the low- and moderate-wavenumber cases²².

One significant flow feature of Chini–Cox solution is that the thermal and vorticity layers on all four edges of a roll are much thinner than the roll itself, e.g. $\delta_x^T/\Gamma \ll 1$ and $\delta_z^T/\Gamma \ll 1$. On the contrary, the heat-exchanger solution requires $\Gamma \ll 1$ so that the horizontal diffusion between neighboring plumes becomes important in the leading order and thereby $\delta_x^T \sim O(\Gamma)$. Hence, the heat-exchanger solution will be valid only at a certain high-wavenumber regime, although the interior solution (4) satisfies (1) mathematically for all k . Below we measure δ_x^T/Γ and δ_z^T/Γ to determine an approximate criterion for convergence of convection rolls to Chini–Cox solution.

As shown in figure 13, both δ_x^T and δ_z^T scale as $Ra^{-1/3}$ for fixed aspect ratios. Interestingly, the data points for different Γ ’s collapse after rescaling and as $Ra \rightarrow \infty$,

$$\Gamma^{1.5}Ra^{1/3} \frac{\delta_x^T}{\Gamma} \simeq 7.62 \quad \text{and} \quad \Gamma^{1.5}Ra^{1/3} \frac{\delta_z^T}{\Gamma} \simeq 5.68. \quad (9)$$

From figures 11–13, we find a good convergence to the Chini–Cox solution is achieved when the ratio of the thickness of the thermal layer to the aspect ratio, i.e. δ^T/Γ , is less than 0.02. Substituting this value into (9) and choosing the stricter criterion, we obtain an approximate region for Chini–Cox solution, $k < k_{CC} \simeq 0.12Ra^{0.22}$. Namely, for fixed k , it requires $Ra > (k/0.12)^{1/0.22}$ to approximately converge to the asymptotic Chini–Cox solution, consistent with our observation that convergence of the asymptotic scalings of Nu and Re is slower at higher k .

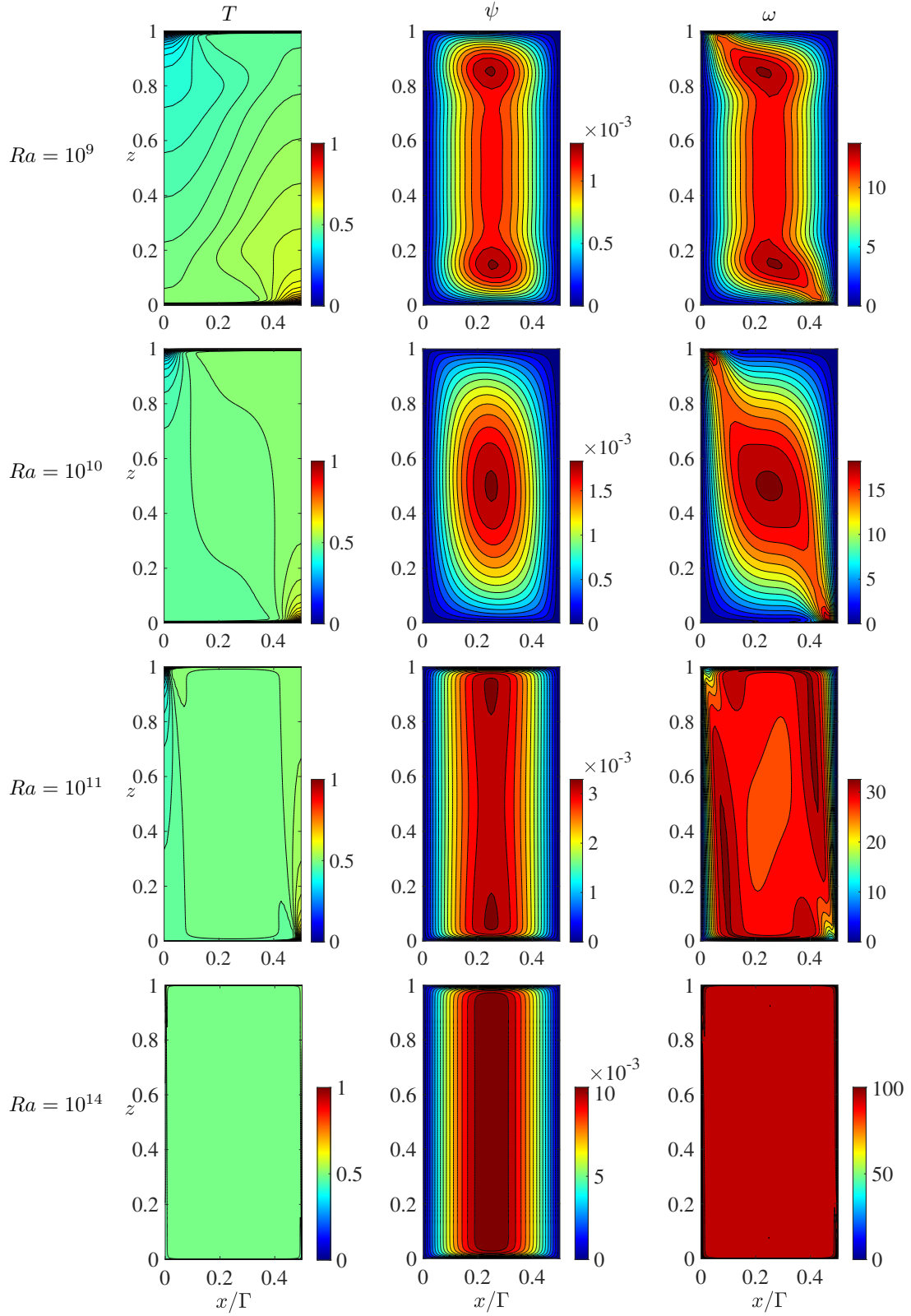


FIG. 8. Contours of (from left to right) T , ψ , and ω for solutions at $Pr = 1$ and $\Gamma = 0.06$ with (from top to bottom) $Ra = 10^9$, 10^{10} , 10^{11} , and 10^{14} . Only the convection roll with counterclockwise circulation is plotted due to the reflection symmetry about $x = \Gamma/2$. At $Ra = 10^9$ and $Pr = 1$, $\Gamma = 0.06 \approx \Gamma_{loc}^* = 0.0608854$, so the convection roll at the top panel exhibits a similar flow pattern with the local Nu -maximizing solution shown in Fig. 3. As Ra increases under fixed Γ , however, it transitions to the Chini–Cox solution.

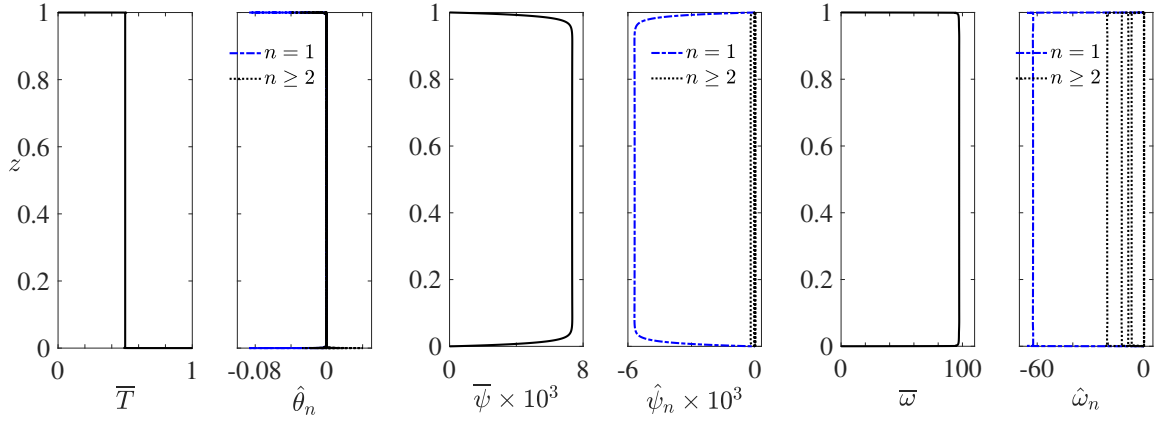


FIG. 9. The z -dependent Fourier components of the solution at $Ra = 10^{14}$ and $Pr = 1$ with $\Gamma = 0.06$. The horizontal-mean components \bar{T} , $\bar{\psi}$, and $\bar{\omega}$ are from a single convection roll with counterclockwise circulation. For fixed Γ , the temperature and vorticity fields are strongly homogenized in the interior at sufficiently large Ra .

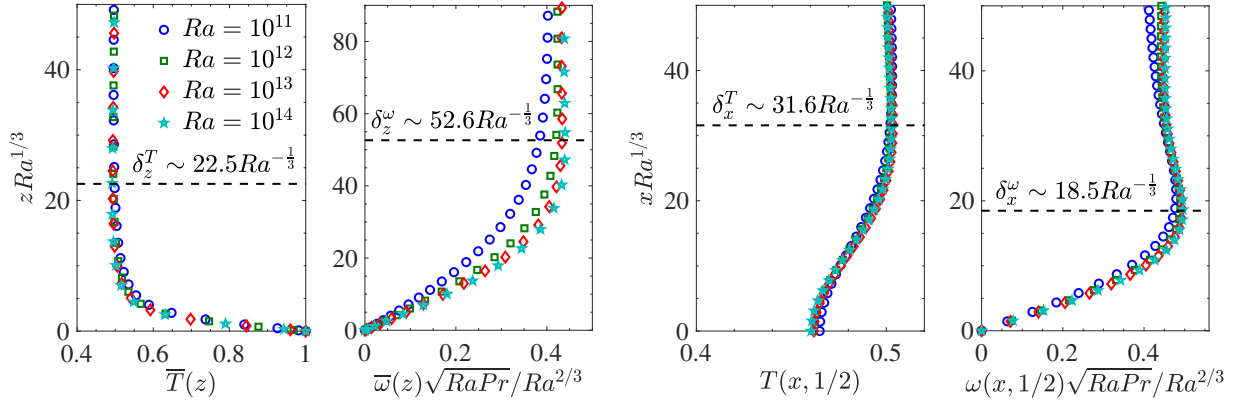


FIG. 10. Scaled spatial structure of temperature T and compensated vorticity ω near the bottom and left side of a convection roll at $Pr = 1$ and $\Gamma = 0.06$. The dashed lines are used to denote the edges of the thermal and vorticity layers—i.e. the first local extrema with $\partial_z = 0$ or $\partial_x = 0$ away from the edges of the roll. The horizontal-mean profiles are from a single convection roll with counterclockwise circulation. The scaled profiles coincide at sufficiently large Ra , confirming that the thicknesses of both the thermal and vorticity layers scale as $Ra^{-1/3}$.

D. Phase diagram in high- Ra - k plane

Figure 14 shows the phase diagram in high- Ra - k plane for steady solutions of 2D Rayleigh–Bénard convection between stress-free boundaries at $Pr = 1$. As discussed above, the high-wavenumber convection rolls bifurcate from the conduction state at $Ra_c = k^4$. Below $k_c = Ra^{1/4}$ is the regime for the heat-exchanger solution. To quantify the proximity of the Blennerhassett–Bassom solution or a given numerically computed steady roll solution to the analytical heat-exchanger solution (4) in the interior, we follow Wen, Corson & Chini²⁰ by introducing the parameter $\gamma = -(Ra/k^4)\partial_z \bar{T}|_{z=1/2}$ that measures the ratio of the mean temperature gradient at the mid-plane to the analytically predicted vertical temperature gradient. The solutions are identical when $\Gamma = 1$; and the Blennerhassett–Bassom solution or the numerical steady roll solution belongs to the class of heat-exchanger solution when $0.99 \leq \Gamma \leq 1$. The comparisons indicate that the Blennerhassett–Bassom solution is valid only in a small re-

gion $k_c > k \geq k_{BB} \simeq 0.97k_c$ and the numerical heat-exchanger solution, i.e. the numerically computed steady roll solution with $0.99 \leq \Gamma \leq 1$, occurs at $k_c > k \geq k_h \simeq 1.32Ra^{0.21}$. At large Ra , $k_{loc}^* = 2\pi/\Gamma_{loc}^* \simeq 0.56Ra^{1/4} \in (k_c, k_h)$, so the local Nu -maximizing solution is naturally a heat-exchanger solution. For $k \geq k_{CC} \simeq 0.12Ra^{0.22}$, the steady convection rolls converge approximately to the Chini–Cox solution. It is seen that k_h and k_{CC} are nearly parallel.

IV. CONCLUSIONS

Recent investigations of 2D Rayleigh–Bénard convection between no-slip boundaries^{18,19,25} reveal that steady roll solutions achieve more heat transport at certain high wavenumbers. In this work we perform a systematic study on the flow structure and heat transport properties of high-wavenumber steady roll solutions in 2D Rayleigh–Bénard convection between stress-free boundaries. In order to elucidate the asymptotic properties of these solutions, we conduct the compu-

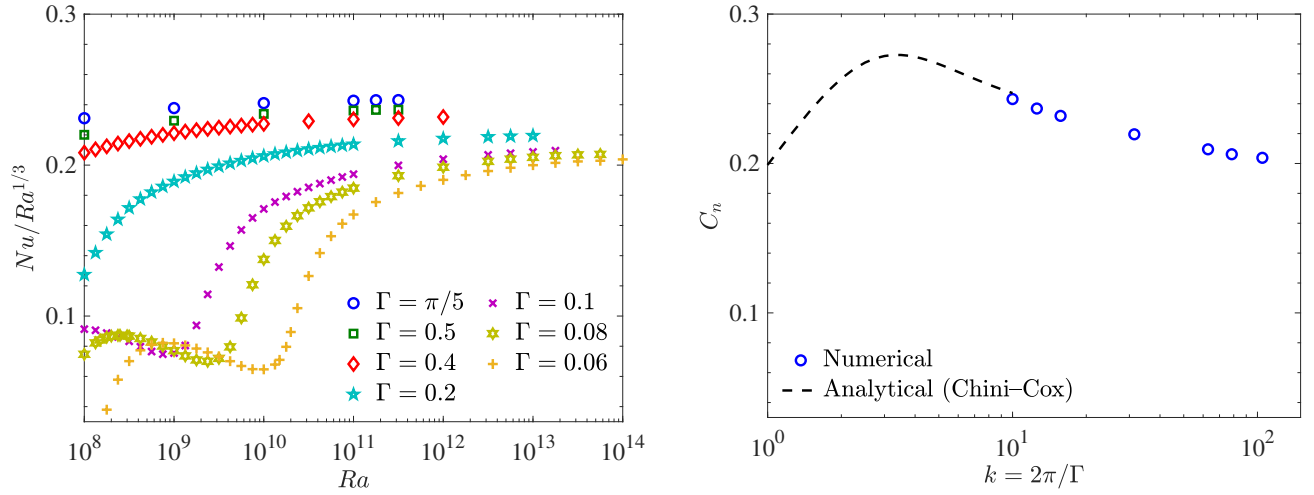


FIG. 11. Left: Compensated plot of Nu vs Ra over a variety of Γ with $Pr = 1$. For fixed Γ , steady convection converges to the Chini–Cox solution as $Ra \rightarrow \infty$, i.e. $Nu \sim C_n(k)Ra^{1/3}$, and this convergence is slower when Γ is smaller. Right: C_n vs k . C_n is computed based on the highest- Ra data.

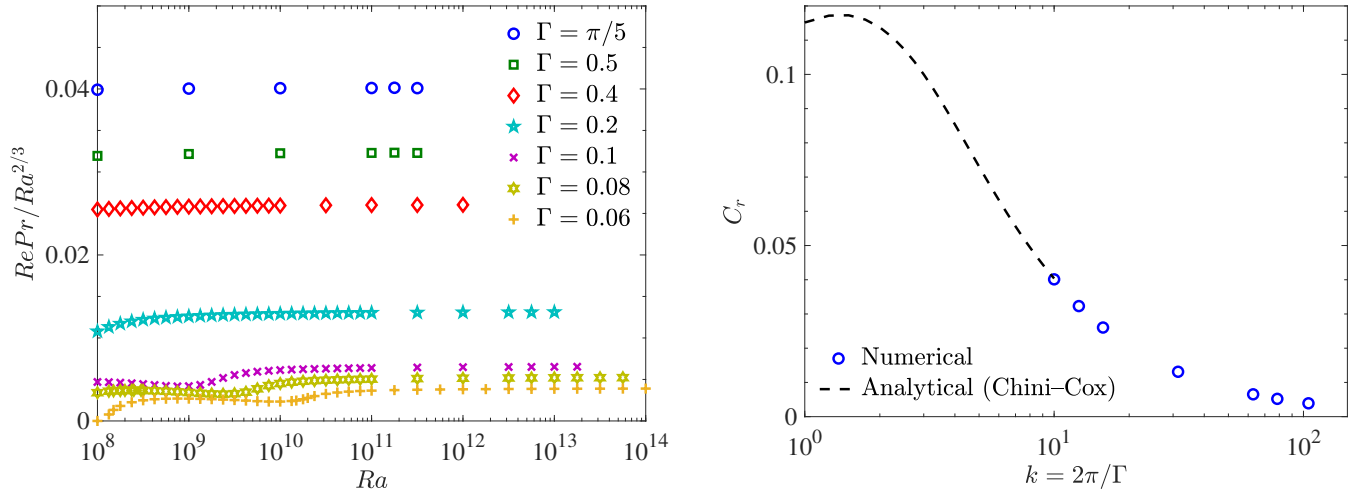


FIG. 12. Left: Compensated plot of Re vs Ra over a variety of Γ with $Pr = 1$. For fixed Γ , steady convection converges to the Chini–Cox solution as $Ra \rightarrow \infty$, i.e. $RePr \sim C_r(k)Ra^{2/3}$, and this convergence is slower when Γ is smaller. Right: C_r vs k . C_r is computed based on the highest- Ra data.

tations using a highly accurate spectral solver over $Ra \in [10^8, 10^{16.5}]$ and $Pr \in [10^{-1}, 10^{3/2}]$. Our numerical results indicate that as $Ra \rightarrow \infty$, a local Nu -maximizing solution exists along the wavenumber $k \simeq \mathcal{O}(Ra^{1/4})$ with $Nu \simeq \mathcal{O}(Ra^{0.29})$ and $RePr \simeq \mathcal{O}(Ra^{2/5})$, similar to the no-slip case with Prandtl number unity. At large Ra , the interior of the local Nu -maximizing solution exhibits a heat-exchanger flow structure, i.e., the horizontal diffusion of heat between neighboring plumes balances the vertical advection of the emergent linear-in- z horizontal-mean temperature profile; near the upper and lower boundaries, however, flow recirculation zones emerge with the thickness decreasing as $\mathcal{O}(Ra^{-0.1})$ and, to a certain extent, reduce the efficiency of heat transport. Our numerical data show that at each large Ra , the steady roll solution, which bifurcates supercritically from the conduction state at $k_c = Ra^{1/4}$, remains the heat-exchanger flow pattern

for $k_c > k \gtrsim 1.32Ra^{0.21}$, while the Blennerhassett–Bassom asymptotic solution is only a weakly nonlinear form of the heat-exchanger solution at $k = k_c + \mathcal{O}(\varepsilon)$.

For fixed aspect ratio Γ , the flow recirculation zones disappear gradually as Ra is increased and the steady solutions eventually converge to the Chini–Cox asymptotic solution so that $Nu = \mathcal{O}(Ra^{1/3})$, $RePr = \mathcal{O}(Ra^{2/3})$, and both the plume and boundary-layer thicknesses scale as $\mathcal{O}(Ra^{-1/3})$. Our numerical data reveal that at large Ra the compensated plume and boundary-layer thicknesses follow a general function of $\Gamma^{1.5}Ra^{1/3}$, allowing us to formulate a criterion for the convergence to the Chini–Cox solution, e.g., $k \lesssim 0.12Ra^{0.22}$ at $Pr = 1$. This work provides a panorama of steady roll solutions—bifurcating from the conduction state—in the high- Ra - k plane for 2D Rayleigh–Bénard convection between stress-free boundaries.

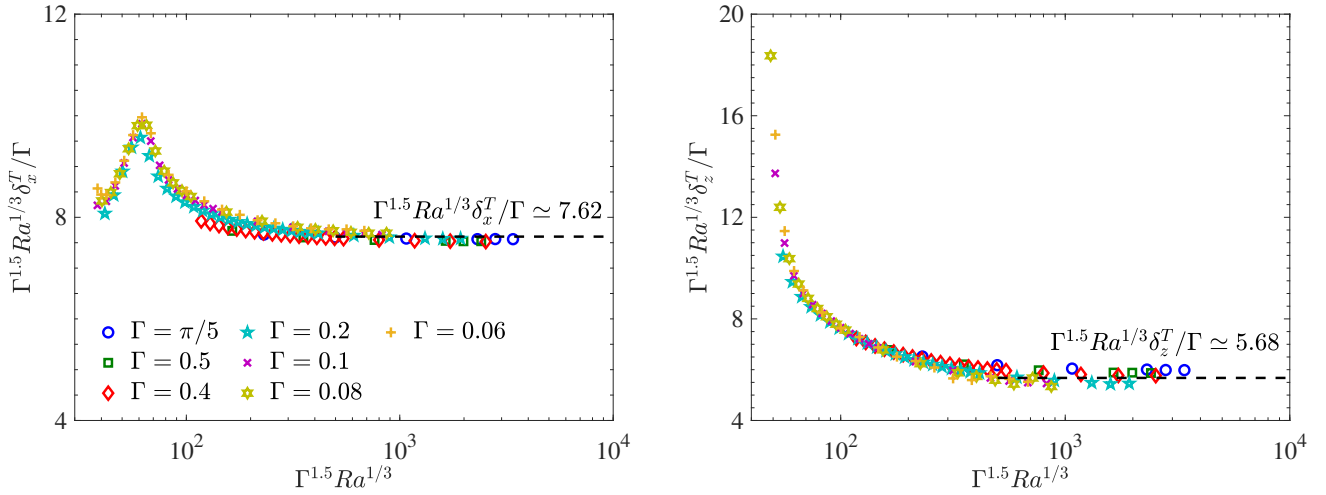


FIG. 13. Compensated plume thickness δ_x (left) and boundary-layer thickness δ_z (right) for steady rolls with $Pr = 1$ over a variety of Γ . For fixed Pr and Γ , both δ_x and δ_z scale as $Ra^{-1/3}$ as $Ra \rightarrow \infty$, namely, $\Gamma^{1.5} Ra^{1/3} \delta_x^T / \Gamma \simeq 7.62$ and $\Gamma^{1.5} Ra^{1/3} \delta_z^T / \Gamma \simeq 5.68$ (dashed lines). For various Γ , the rescaled δ_x and δ_z data collapse as function of $\Gamma^{1.5} Ra^{1/3}$.

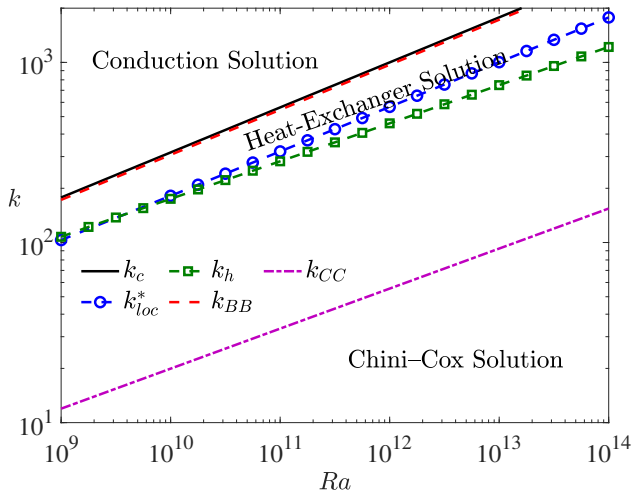


FIG. 14. Phase diagram in high- Ra - k plane at $Pr = 1$. $k > k_c = Ra^{1/4}$: conduction solution; $k_c > k > k_{BB} \simeq 0.97k_c$: Blennerhassett–Bassom solution from weakly nonlinear analysis; $k_c > k > k_h \simeq 1.32Ra^{0.21}$: numerical heat-exchanger solution; $k < k_{CC} \simeq 0.12Ra^{0.22}$: Chini–Cox solution from asymptotic analysis. At large Ra , the local Nu -maximizing solution is naturally a heat-exchanger solution since $k_{loc}^* = 2\pi/\Gamma_{loc}^* \approx 0.56Ra^{1/4} \in (k_h, k_c)$.

¹F. P. Incropera, *Liquid cooling of electronic devices by single-phase convection*, Vol. 3 (Wiley-Interscience, 1999).

²L. Ma, J. Li, S. Ji, and H. Chang, “Turbulent convection experiment at high Rayleigh number to support CAPI400 IVR strategy,” *Nuclear Engineering and Design* **292**, 69–75 (2015).

³J. C. Wyngaard, “Atmospheric turbulence,” *Annual Review of Fluid Mechanics* **24**, 205–234 (1992).

⁴B. Stevens, “Atmospheric moist convection,” *Annu. Rev. Earth Planet. Sci.* **33**, 605–643 (2005).

⁵P. A. O’Gorman and J. G. Dwyer, “Using machine learning to parameterize moist convection: Potential for modeling of climate, climate change, and extreme events,” *Journal of Advances in Modeling Earth Systems* **10**, 2548–2563 (2018).

⁶J. Marshall and F. Schott, “Open-ocean convection: Observations, theory, and models,” *Reviews of Geophysics* **37**, 1–64 (1999).

⁷L. P. Kadanoff, “Turbulent heat flow: Structures and scaling,” *Physics Today* **54**, 34–39 (2001).

⁸F. Chillà and J. Schumacher, “New perspectives in turbulent Rayleigh–Bénard convection,” *The European Physical Journal E* **35**, 58 (2012).

⁹J. Schumacher and K. R. Sreenivasan, “Colloquium: Unusual dynamics of convection in the sun,” *Reviews of Modern Physics* **92**, 041001 (2020).

¹⁰G. M. Vasil, K. Julien, and N. A. Featherstone, “Rotation suppresses giant-scale solar convection,” *Proceedings of the National Academy of Sciences* **118**, e2022518118 (2021).

¹¹L. Rayleigh, “On convection currents in a horizontal layer of fluid, when the higher temperature is on the under side,” *Philosophical Magazine* **32**, 529–546 (1916).

¹²C. R. Doering, “Turning up the heat in turbulent thermal convection,” *Proceedings of the National Academy of Sciences USA* **117**, 9671–9673 (2020).

¹³H. Jeffreys, “Some cases of instability in fluid motion,” *Proceedings of the Royal Society A* **118**, 195–208 (1928).

¹⁴E. van der Poel, R. Ostilla-Mónico, R. Verzicco, and D. Lohse, “Effect of velocity boundary conditions on the heat transfer and flow topology in two-dimensional Rayleigh–Bénard convection,” *Physical Review E* **90**, 013017 (2014).

¹⁵D. Goluskin, H. Johnston, G. R. Flierl, and E. A. Spiegel, “Convectively driven shear and decreased heat flux,” *Journal of Fluid Mechanics* **759**, 360–385 (2014).

¹⁶Q. Wang, K. L. Chong, R. J. A. M. Stevens, R. Verzicco, and D. Lohse, “From zonal flow to convection rolls in Rayleigh–Bénard convection with free-slip plates,” *Journal of Fluid Mechanics* **905**, A21 (2020).

¹⁷P. Winchester, P. D. Howell, and V. Dallas, “The onset of zonal modes in two-dimensional rayleigh–bénard convection,” *Journal of Fluid Mechanics* **939** (2022).

¹⁸F. Waleffe, A. Boonkasame, and L. M. Smith, “Heat transport by coherent Rayleigh–Bénard convection,” *Physics of Fluids* **27**, 051702 (2015).

¹⁹D. Sondak, L. M. Smith, and F. Waleffe, “Optimal heat transport solutions for Rayleigh–Bénard convection,” *Journal of Fluid Mechanics* **784**, 565–595 (2015).

²⁰B. Wen, L. T. Corson, and G. P. Chini, “Structure and stability of steady porous medium convection at large Rayleigh number,” *Journal of Fluid Mechanics* **772**, 197–224 (2015).

²¹B. Wen and G. P. Chini, “Inclined porous medium convection at large Rayleigh number,” *Journal of Fluid Mechanics* **837**, 670–702 (2018).

²²B. Wen, D. Goluskin, M. LeDuc, G. P. Chini, and C. R. Doering, “Steady Rayleigh–Bénard convection between stress-free boundaries,” *Journal of*

- Fluid Mechanics **905**, R4 (2020).
- ²³P. Kooloth, D. Sondak, and L. M. Smith, “Coherent solutions and transition to turbulence in two-dimensional Rayleigh–Bénard convection,” *Phys. Rev. Fluids* **6**, 013501 (2021).
- ²⁴Z. Ding and J. Wu, “Coherent heat transport in two-dimensional penetrative rayleigh–bénard convection,” *Journal of Fluid Mechanics* **920** (2021).
- ²⁵B. Wen, D. Goluskin, and C. R. Doering, “Steady Rayleigh–Bénard convection between no-slip boundaries,” *Journal of Fluid Mechanics* **933**, R4 (2022).
- ²⁶S. Motoki, G. Kawahara, and M. Shimizu, “Multi-scale steady solution for Rayleigh–Bénard convection,” *Journal of Fluid Mechanics* **914**, A14 (2021).
- ²⁷S. Motoki, G. Kawahara, and M. Shimizu, “Steady thermal convection representing the ultimate scaling,” *Philosophical Transactions of the Royal Society A* **380**, 20210037 (2022).
- ²⁸M. Nagata, “Three-dimensional finite-amplitude solutions in plane Couette flow: bifurcation from infinity,” *Journal of Fluid Mechanics* **217**, 519–527 (1990).
- ²⁹F. Waleffe, “Three-dimensional coherent states in plane shear flows,” *Physical Review Letters* **81**, 4140 (1998).
- ³⁰H. Wedin and R. R. Kerswell, “Exact coherent structures in pipe flow: travelling wave solutions,” *Journal of Fluid Mechanics* **508**, 2–5 (2004).
- ³¹J. F. Gibson, J. Halcrow, and P. Cvitanović, “Visualizing the geometry of state space in plane Couette flow,” *Journal of Fluid Mechanics* **611**, 107–130 (2008).
- ³²B. Suri, L. Kageorge, R. O. Grigoriev, and M. F. Schatz, “Capturing turbulent dynamics and statistics in experiments with unstable periodic orbits,” *Physical Review Letters* **125**, 064501 (2020).
- ³³M. A. Ahmed and A. S. Sharma, “Basis for finding exact coherent states,” *Physical Review E* **101**, 012213 (2020).
- ³⁴M. D. Graham and D. Floryan, “Exact coherent states and the nonlinear dynamics of wall-bounded turbulent flows,” *Annual Review of Fluid Mechanics* **53** (2021).
- ³⁵M. L. Olson, D. Goluskin, W. W. Schultz, and C. R. Doering, “Heat transport bounds for a truncated model of Rayleigh–Bénard convection via polynomial optimization,” *Physica D* **415**, 132748 (2021).
- ³⁶C. R. Doering and P. Constantin, “Variational bounds on energy dissipation in incompressible flows. iii. convection,” *Physical Review E* **53**, 5957–5981 (1996).
- ³⁷S. C. Plasting and R. R. Kerswell, “Improved upper bound on the energy dissipation rate in plane Couette flow: the full solution to Busse’s problem and the Constantin–Doering–Hopf problem with one-dimensional background field,” *J. Fluid Mech.* **477**, 363–379 (2003).
- ³⁸C. R. Doering, F. Otto, and M. G. Reznikoff, “Bounds on vertical heat transport for infinite-Prandtl-number Rayleigh–Bénard convection,” *J. Fluid Mech.* **560**, 229–241 (2006).
- ³⁹J. P. Whitehead and C. R. Doering, “Ultimate state of two-dimensional Rayleigh–Bénard convection between free-slip fixed-temperature boundaries,” *Phys. Rev. Lett.* **106**, 244501 (2011).
- ⁴⁰G. P. Chini and S. M. Cox, “Large Rayleigh number thermal convection: Heat flux predictions and strongly nonlinear solutions,” *Physics of Fluids* **21**, 083603 (2009).
- ⁴¹P. Blennerhassett and A. P. Bassom, “Nonlinear high-wavenumber Bénard convection,” *IMA Journal of Applied Mathematics* **52**, 51–77 (1994).
- ⁴²J. P. Boyd, *Chebyshev and Fourier Spectral Methods*, 2nd ed. (Dover, New York, 2000).
- ⁴³L. Trefethen, *Spectral Methods in MATLAB* (SIAM, 2000).
- ⁴⁴D. R. Hewitt, J. A. Neufeld, and J. R. Lister, “Ultimate regime of high Rayleigh number convection in a porous medium,” *Physical Review Letters* **108**, 224503 (2012).
- ⁴⁵P. Hassanzadeh, G. P. Chini, and C. R. Doering, “Wall to wall optimal transport,” *Journal of fluid mechanics* **751**, 627–662 (2014).
- ⁴⁶A. N. Souza, I. Tobasco, and C. R. Doering, “Wall-to-wall optimal transport in two dimensions,” *Journal of Fluid Mechanics* **889** (2020).
- ⁴⁷E. A. Spiegel, “On the Malkus theory of turbulence,” *Mécanique de la turbulence*, Centre National de la Recherche Scientifique, Paris, 181–201 (1962).